Three-jet production in diffractive deep inelastic scattering at HERA

ZEUS Collaboration

Abstract

Three-jet production in the reaction $ep \to eXp$ has been studied with the ZEUS detector at HERA using an integrated luminosity of 42.74 pb^{-1}. The data were measured in the kinematic region $5 < Q^2 < 100$ GeV^2, $200 < W < 250$ GeV and $23 < M_X < 40$ GeV. The diffractive signal was selected by requiring a large rapidity gap in the outgoing proton direction. Jets were reconstructed in the centre-of-mass system of X using the exclusive k_T-algorithm. A sample of three-jet events in diffraction has been identified. Differential cross sections were measured as a function of the jet pseudorapidity and jet transverse momentum with respect to the virtual photon-Pomeron axis. The jets going in the Pomeron direction are broader than those going in the virtual-photon direction. This is consistent with models predicting that gluons are predominantly produced in the Pomeron direction and quarks in the virtual-photon direction.

The ZEUS Collaboration

S. Chekanov, M. Derrick, D. Krakauer, S. Magill, B. Musgrave, A. Pellegrino, J. Repond, R. Yoshida
Argonne National Laboratory, Argonne, IL, USA [n]

M.C.K. Mattingly
Andrews University, Berrien Springs, MI, USA

P. Antonioli, G. Bari, M. Basile, L. Bellagamba, D. Boscherini[1], A. Bruni, G. Bruni, G. Cara Romeo, L. Cifarelli[2], F. Cindolo, A. Contin, M. Corradi, S. De Pasquale, P. Giusti, G. Iacobucci, G. Levi, A. Margotti, T. Massam, R. Nania, F. Palmonari, A. Pesci, G. Sartorelli, A. Zichichi
University and INFN Bologna, Bologna, Italy [e]

G. Aghuzumtsyan, I. Brock, S. Goers, H. Hartmann, E. Hilger, P. Irrgang, H.-P. Jakob, A. Kappes[3], U.F. Katz[4], R. Kerger, O. Kind, E. Paul, J. Rautenberg, H. Schnurbusch, A. Stifutkin, J. Tandler, K.C. Voss, A. Weber, H. Wieber
Physikalisches Institut der Universität Bonn, Bonn, Germany [b]

D.S. Bailey[5], N.H. Brook[5], J.E. Cole, B. Foster, G.P. Heath, H.F. Heath, S. Robins, E. Rodrigues[6], J. Scott, R.J. Tapper, M. Wing
H.H. Wills Physics Laboratory, University of Bristol, Bristol, U.K. [m]

M. Capua, A. Mastroberardino, M. Schioppa, G. Susinno
Calabria University, Physics Dept.and INFN, Cosenza, Italy [e]

H.Y. Jeoung, J.Y. Kim, J.H. Lee, I.T. Lim, K.J. Ma, M.Y. Pac[7]
Chonnam National University, Kwangju, Korea [g]

A. Caldwell, M. Helbich, W. Liu, X. Liu, B. Mellado, S. Paganis, S. Sampson, W.B. Schmidke, F. Sciulli
Columbia University, Nevis Labs., Irvington on Hudson, N.Y., USA [o]

J. Chwastowski, A. Eskreys, J. Figiel, K. Klimek[8], K. Olkiewicz, M.B. Przybycień[9], P. Stopa, L. Zawiejski
Inst. of Nuclear Physics, Cracow, Poland [i]

B. Bednarek, K. Jeleń, D. Kisielewska, A.M. Kowal[10], M. Kowal, T. Kowalski, B. Mindur, M. Przybycień, E. Rulikowska-Zarębska, L. Suszycki, D. Szuba
Faculty of Physics and Nuclear Techniques, Academy of Mining and Metallurgy, Cracow, Poland [i]

A. Kotański
Jagellonian Univ., Dept. of Physics, Cracow, Poland

L.A.T. Bauerdick[11], U. Behrens, K. Borras, V. Chiochia, J. Crittenden[12], D. Dannheim, K. Desler, G. Drews, A. Fox-Murphy, U. Fricke, A. Geiser, F. Goebel, P. Göttlicher, R. Graciani, T. Haas, W. Hain, G.F. Hartner, K. Hebbel, S. Hillert, W. Koch[13]†, U. Kötz, H. Kowalski, H. Labes, B. Löhr, R. Mankel, J. Martens, M. Martínez, M. Milite, M. Moritz, D. Notz, M.C. Petrucci, A. Polini, U. Schneekloth, F. Selonke, S. Stonjek, G. Wolf, U. Wollmer, J.J. Whitmore[14], R. Wichmann[15], C. Youngman, W. Zeuner
Deutsches Elektronen-Synchrotron DESY, Hamburg, Germany

C. Coldewey, A. Lopez-Duran Viani, A. Meyer, S. Schlenstedt
DESY Zeuthen, Zeuthen, Germany

G. Barbagli, E. Gallo, P. G. Pelfer
University and INFN, Florence, Italy [e]

A. Bamberger, A. Benen, N. Coppola, P. Markun, H. Raach[16], S. Wölfle
Fakultät für Physik der Universität Freiburg i.Br., Freiburg i.Br., Germany [b]

M. Bell, P.J. Bussey, A.T. Doyle, C. Glasman, S.W. Lee[17], A. Lupi, G.J. McCance, D.H. Saxon, I.O. Skillicorn
Dept. of Physics and Astronomy, University of Glasgow, Glasgow, U.K. [m]

B. Bodmann, N. Gendner, U. Holm, H. Salehi, K. Wick, A. Yildirim, A. Ziegler
Hamburg University, I. Institute of Exp. Physics, Hamburg, Germany [b]

T. Carli, A. Garfagnini, I. Gialas[18], E. Lohrmann
Hamburg University, II. Institute of Exp. Physics, Hamburg, Germany [b]

C. Foudas, R. Gonçalo[6], K.R. Long, F. Metlica, D.B. Miller, A.D. Tapper, R. Walker
Imperial College London, High Energy Nuclear Physics Group, London, U.K. [m]

P. Cloth, D. Filges
Forschungszentrum Jülich, Institut für Kernphysik, Jülich, Germany

M. Kuze, K. Nagano, K. Tokushuku[19], S. Yamada, Y. Yamazaki
Institute of Particle and Nuclear Studies, KEK, Tsukuba, Japan [f]

A.N. Barakbaev, E.G. Boos, N.S. Pokrovskiy, B.O. Zhautykov
Institute of Physics and Technology of Ministry of Education and Science of Kazakhstan, Almaty, Kazakhstan

S.H. Ahn, S.B. Lee, S.K. Park
Korea University, Seoul, Korea [g]

H. Lim[17], D. Son
Kyungpook National University, Taegu, Korea [g]

F. Barreiro, G. García, O. González, L. Labarga, J. del Peso, I. Redondo[20], J. Terrón, M. Vázquez
Univer. Autónoma Madrid, Depto de Física Teórica, Madrid, Spain [l]

M. Barbi, A. Bertolin, F. Corriveau, A. Ochs, S. Padhi, D.G. Stairs
McGill University, Dept. of Physics, Montréal, Québec, Canada [a]

T. Tsurugai
Meiji Gakuin University, Faculty of General Education, Yokohama, Japan

A. Antonov, V. Bashkirov[21], P. Danilov, B.A. Dolgoshein, D. Gladkov, V. Sosnovtsev, S. Suchkov
Moscow Engineering Physics Institute, Moscow, Russia [k]

R.K. Dementiev, P.F. Ermolov, Yu.A. Golubkov, I.I. Katkov, L.A. Khein, N.A. Korotkova, I.A. Korzhavina, V.A. Kuzmin, B.B. Levchenko, O.Yu. Lukina, A.S. Proskuryakov, L.M. Shcheglova, A.N. Solomin, N.N. Vlasov, S.A. Zotkin
Moscow State University, Institute of Nuclear Physics, Moscow, Russia [k]

C. Bokel, J. Engelen, S. Grijpink, E. Maddox, E. Koffeman, P. Kooijman, S. Schagen, E. Tassi, H. Tiecke, N. Tuning, J.J. Velthuis, L. Wiggers, E. de Wolf
NIKHEF and University of Amsterdam, Amsterdam, Netherlands [h]

N. Brümmer, B. Bylsma, L.S. Durkin, J. Gilmore, C.M. Ginsburg, C.L. Kim, T.Y. Ling
Ohio State University, Physics Department, Columbus, Ohio, USA [n]

S. Boogert, A.M. Cooper-Sarkar, R.C.E. Devenish, J. Ferrando, J. Große-Knetter[22], T. Matsushita, M. Rigby, O. Ruske[23], M.R. Sutton, R. Walczak
Department of Physics, University of Oxford, Oxford U.K. [m]

R. Brugnera, R. Carlin, F. Dal Corso, S. Dusini, S. Limentani, A. Longhin, A. Parenti, M. Posocco, L. Stanco, M. Turcato
Dipartimento di Fisica dell' Università and INFN, Padova, Italy [e]

L. Adamczyk[24], L. Iannotti[24], B.Y. Oh, P.R.B. Saull[24], W.S. Toothacker[13]†
Pennsylvania State University, Dept. of Physics, University Park, PA, USA [o]

Y. Iga
Polytechnic University, Sagamihara, Japan [f]

G. D'Agostini, G. Marini, A. Nigro
Dipartimento di Fisica, Univ. 'La Sapienza' and INFN, Rome, Italy [e]

C. Cormack, J.C. Hart, N.A. McCubbin
Rutherford Appleton Laboratory, Chilton, Didcot, Oxon, U.K. [m]

D. Epperson, C. Heusch, H.F.-W. Sadrozinski, A. Seiden, D.C. Williams
University of California, Santa Cruz, CA, USA [n]

I.H. Park
Seoul National University, Seoul, Korea

N. Pavel
Fachbereich Physik der Universität-Gesamthochschule Siegen, Germany [b]

H. Abramowicz, S. Dagan, A. Gabareen, S. Kananov, A. Kreisel, A. Levy
Raymond and Beverly Sackler Faculty of Exact Sciences, School of Physics, Tel-Aviv University, Tel-Aviv, Israel [d]

T. Abe, T. Fusayasu, T. Kohno, K. Umemori, T. Yamashita
Department of Physics, University of Tokyo, Tokyo, Japan [f]

R. Hamatsu, T. Hirose, M. Inuzuka, S. Kitamura[25], K. Matsuzawa, T. Nishimura
Tokyo Metropolitan University, Dept. of Physics, Tokyo, Japan [f]

M. Arneodo[26], N. Cartiglia, R. Cirio, M. Costa, M.I. Ferrero, S. Maselli, V. Monaco, C. Peroni, M. Ruspa, R. Sacchi, A. Solano, A. Staiano
Università di Torino, Dipartimento di Fisica Sperimentale and INFN, Torino, Italy [e]

D.C. Bailey, C.-P. Fagerstroem, R. Galea, T. Koop, G.M. Levman, J.F. Martin, A. Mirea, A. Sabetfakhri
University of Toronto, Dept. of Physics, Toronto, Ont., Canada [a]

J.M. Butterworth, C. Gwenlan, R. Hall-Wilton, M.E. Hayes[22], E.A. Heaphy, T.W. Jones, J.B. Lane, M.S. Lightwood, B.J. West
University College London, Physics and Astronomy Dept., London, U.K. [m]

J. Ciborowski[27], R. Ciesielski, G. Grzelak, R.J. Nowak, J.M. Pawlak, B. Smalska[28], T. Tymieniecka[29], J. Ukleja[29], J.A. Zakrzewski, A.F. Żarnecki
Warsaw University, Institute of Experimental Physics, Warsaw, Poland [i]

M. Adamus, P. Plucinski, J. Sztuk
Institute for Nuclear Studies, Warsaw, Poland [i]

O. Deppe[30], Y. Eisenberg, L.K. Gladilin[31], D. Hochman, U. Karshon
Weizmann Institute, Department of Particle Physics, Rehovot, Israel [c]

J. Breitweg, D. Chapin, R. Cross, D. Kçira, S. Lammers, D.D. Reeder, A.A. Savin, W.H. Smith
University of Wisconsin, Dept. of Physics, Madison, WI, USA [n]

A. Deshpande, S. Dhawan, V.W. Hughes P.B. Straub
Yale University, Department of Physics, New Haven, CT, USA [n]

S. Bhadra, C.D. Catterall, W.R. Frisken, M. Khakzad, S. Menary
York University, Dept. of Physics, Toronto, Ont., Canada [a]

[1] now visiting scientist at DESY
[2] now at Univ. of Salerno and INFN Napoli, Italy
[3] supported by the GIF, contract I-523-13.7/97
[4] on leave of absence at University of Erlangen-Nürnberg, Germany
[5] PPARC Advanced fellow
[6] supported by the Portuguese Foundation for Science and Technology (FCT)
[7] now at Dongshin University, Naju, Korea
[8] supported by the Polish State Committee for Scientific Research, grant no. 5 P-03B 08720
[9] now at Northwestern Univ., Evaston/IL, USA
[10] supported by the Polish State Committee for Scientific Research, grant no. 5 P-03B 13720
[11] now at Fermilab, Batavia/IL, USA
[12] on leave of absence from Bonn University
[13] deceased
[14] on leave from Penn State University, USA
[15] partly supported by Penn State University and GIF, contract I-523-013.07/97
[16] supported by DESY
[17] partly supported by an ICSC-World Laboratory Björn H. Wiik Scholarship
[18] Univ. of the Aegean, Greece
[19] also at University of Tokyo
[20] supported by the Comunidad Autonoma de Madrid
[21] now at Loma Linda University, Loma Linda, CA, USA
[22] now at CERN, Geneva, Switzerland
[23] now at IBM Global Services, Frankfurt/Main, Germany
[24] partly supported by Tel Aviv University
[25] present address: Tokyo Metropolitan University of Health Sciences, Tokyo 116-8551, Japan
[26] now also at Università del Piemonte Orientale, I-28100 Novara, Italy
[27] and Łódź University, Poland
[28] supported by the Polish State Committee for Scientific Research, grant no. 2 P-03B 00219
[29] supported by the Polish State Committee for Scientific Research, grant no. 5 P-03B 09820
[30] now at EVOTEC BioSystems AG, Hamburg, Germany
[31] on leave from MSU, partly supported by University of Wisconsin via the U.S.-Israel BSF

[a] supported by the Natural Sciences and Engineering Research Council of Canada (NSERC)
[b] supported by the German Federal Ministry for Education and Science, Research and Technology (BMBF), under contract numbers 057BN19P, 057FR19P, 057HH19P, 057HH29P, 057SI75I
[c] supported by the MINERVA Gesellschaft für Forschung GmbH, the Israel Science Foundation, the U.S.-Israel Binational Science Foundation, the Israel Ministry of Science and the Benozyio Center for High Energy Physics
[d] supported by the German-Israeli Foundation, the Israel Science Foundation, and by the Israel Ministry of Science
[e] supported by the Italian National Institute for Nuclear Physics (INFN)
[f] supported by the Japanese Ministry of Education, Science and Culture (the Monbusho) and its grants for Scientific Research
[g] supported by the Korean Ministry of Education and Korea Science and Engineering Foundation
[h] supported by the Netherlands Foundation for Research on Matter (FOM)
[i] supported by the Polish State Committee for Scientific Research, grant no. 2P03B04616, 620/E-77/SPUB-M/DESY/P-03/DZ 247/2000 and 112/E-356/SPUB-M/DESY/P-03/DZ 3001/2000
[j] partially supported by the German Federal Ministry for Education and Science, Research and Technology (BMBF)
[k] supported by the Fund for Fundamental Research of Russian Ministry for Science and Education and by the German Federal Ministry for Education and Science, Research and Technology (BMBF)
[l] supported by the Spanish Ministry of Education and Science through funds provided by CICYT
[m] supported by the Particle Physics and Astronomy Research Council, UK
[n] supported by the US Department of Energy
[o] supported by the US National Science Foundation

1 Introduction

One of the most important results from the ep collider HERA is the observation that about 10% of deep inelastic scattering (DIS) events exhibit a large rapidity gap (LRG) between the direction of the proton beam and that of the first significant energy deposition in the detector [1]. These LRG events, $ep \to eXN$, result predominantly from the diffractive dissociation of the virtual photon, $\gamma^* p \to Xp$, and have been interpreted in terms of the exchange of a colour-singlet object known as the Pomeron ($I\!P$), introduced to describe the energy dependence of total cross sections in hadron-hadron scattering [2].

The HERA data [3, 4] have been analysed in terms of a diffractive structure function, F_2^D [5], defined in analogy with the proton structure function, F_2. The results are consistent with a "resolved Pomeron" model where F_2^D factorises into a Regge-inspired Pomeron flux and a Pomeron structure function. The latter has been analysed [3] using the DGLAP evolution equations. The extracted parton densities are dominated by gluons.

Alternatively, a number of QCD models [6] has been proposed to describe diffraction in DIS. In these models, the virtual photon dissociates into a $q\overline{q}$ or $q\overline{q}g$ state that interacts with the proton by the exchange of a gluon ladder. The diffractive cross section can then be formulated in terms of contributions from $q\overline{q}$ and $q\overline{q}g$ final states. The $q\overline{q}g$ component is expected to dominate the diffractive cross section at high masses, M_X [7, 8, 9].

An important feature of the three-parton final state in both classes of models is that, in the rest frame of the system X ($\gamma^* I\!P$ centre-of-mass system for the resolved Pomeron model), the $q\overline{q}$ system tends to populate the virtual-photon hemisphere, while the gluon is emitted in the opposite direction (the Pomeron direction in the resolved Pomeron model). In the resolved Pomeron model, the gluon is the remnant of the Pomeron left after the boson-gluon fusion process has produced a $q\overline{q}$ pair; as a remnant, it follows the original Pomeron direction. In dipole models, to leading order, the gluon in the $q\overline{q}g$ fluctuation from the virtual photon either couples directly to the exchanged gluon ladder or emerges from it, depending on the reference frame. In this case also, therefore, it follows the direction of the gluon ladder ($\equiv$ Pomeron in resolved Pomeron model) and the $q\overline{q}$ pair carries on in the direction of the virtual photon.

Studies of the hadronic final state and jet production in diffractive interactions have been presented by both H1 [10] and ZEUS [11]. In this paper, the jet-like structure of the hadronic final state is studied with the aim of isolating three-parton final states by selecting three-jet events. As was already observed in e^+e^- experiments [12], three-jet topologies can be clearly separated only for centre-of-mass energies above about 20 GeV. The measurements are thus performed in a restricted phase-space region populated by high-mass diffractive systems. Such systems are a small fraction of the total diffractive cross section. They are separated from a substantial background of non-diffractive processes by requiring a large rapidity gap. A search is made for jets using an algorithm that allows the study of jet configurations aligned with respect to the $\gamma^* I\!P$ axis and ensures good parton-hadron correlations. The properties of the three-jet final states are used to test the expectation that the gluon from the dominant $q\overline{q}g$ contribution is emitted in the Pomeron direction. Cross sections are presented as a function of the jet pseudorapidity and jet transverse momentum with respect to the $\gamma^* I\!P$ axis. In addition, the internal structure of the jets is measured for jets found in either the photon or the Pomeron directions, with the aim of distinguishing between quark- and gluon-initiated jets. The different measurements are compared to models of diffraction in DIS.

2 Experimental setup

The data were collected with the ZEUS detector at HERA during 1998-2000 when HERA collided 27.6 GeV electrons or positrons[1] on 920 GeV protons. A total of 7.96 ± 0.14 pb^{-1} of e^-p data and 34.78 ± 0.87 pb^{-1} of e^+p data was used. A detailed description of the ZEUS detector can be found elsewhere [13, 14]. A brief outline of the most relevant components for this analysis is given below.

The ZEUS high-resolution uranium-scintillator calorimeter (CAL) [15] covers 99.7% of the total solid angle. It is divided into three parts with respect to the polar angle[2] as viewed from the nominal interaction point: forward (FCAL), rear (RCAL) and barrel (BCAL) calorimeters. Each part is subdivided longitudinally into electromagnetic (EMC) and hadronic (HAC) sections. The CAL energy resolution, as measured in test-beams, is $\sigma(E)/E = 0.18/\sqrt{E\ (\mathrm{GeV})}$ for positrons and $\sigma(E)/E = 0.35/\sqrt{E\ (\mathrm{GeV})}$ for hadrons.

Charged particles were tracked by the central tracking detector (CTD) [16], which operates in a magnetic field of 1.43 T provided by a thin superconducting coil. The CTD is a drift chamber consisting of 72 cylindrical layers, organised in 9 superlayers, covering the region $15^\circ < \theta < 164^\circ$. The transverse momentum resolution for full-length tracks is $\sigma(p_t)/p_t = 0.0058p_t \oplus 0.0065 \oplus 0.0014/p_t$, with p_t in GeV.

In 1998, a Forward Plug Calorimeter (FPC) [17] was installed in the 20×20 cm^2 beam hole of the FCAL with a small hole of radius 3.15 cm in the centre of the FPC to accommodate the beam pipe. This increased the forward calorimetric coverage by about 1 unit of pseudorapidity to $-3.8 \leq \eta \leq 5$. The FPC consisted of a lead-scintillator sandwich calorimeter divided into electromagnetic and hadronic sections which were read out separately by wavelength-shifting fibres and photomultipliers. The EMC (HAC) sections were segmented into cells of 2.4×2.4 cm^2 (4.8×4.8 cm^2) area and constituted a total of 76 read-out channels. The energy resolution was $\sigma_E/E = 0.41/\sqrt{E} \oplus 0.062$ and $\sigma_E/E = 0.65/\sqrt{E} \oplus 0.06$ for positrons and pions, respectively, where the energies are measured in units of GeV [17].

The small-angle rear tracking detector (SRTD) [18] was used to measure the position of those positrons scattered at a sufficiently small angle to strike it. It consists of two planes of scintillator strips attached to the front face of the RCAL. The SRTD signals resolve single minimum-ionizing particles and provide a position resolution of 0.3 cm. The position of those positrons falling outside the SRTD acceptance was measured in the CAL.

The luminosity was measured via the positron-proton bremsstrahlung process, $ep \to e\gamma p$, using a lead-scintillator calorimeter (LUMI) [19] located at $Z = -107$ m in the HERA tunnel.

[1] Hereafter "positron" is used to refer to both electron and positron beams. For the Q^2 range studied, e^-p and e^+p scattering are assumed to give identical results since contributions from Z^0 exchange are negligible.

[2] The ZEUS coordinate system is a right-handed Cartesian system, with the Z axis pointing in the proton beam direction, referred to as the "forward direction", and the X axis pointing left towards the centre of HERA. The coordinate origin is at the nominal interaction point. The pseudorapidity is defined as $\eta = -\ln(\tan\frac{\theta}{2})$, where the polar angle, θ, is measured with respect to the proton beam direction.

3 Kinematics

The kinematics of inclusive deep inelastic scattering $e(k)\ p(P) \to e(k') + anything$ is described by any two of the following variables:

$$Q^2 = -q^2 = -(k-k')^2, \quad x = \frac{Q^2}{2P\cdot q}, \quad y = \frac{P\cdot q}{P\cdot k}, \quad W^2 = \frac{Q^2(1-x)}{x} + m_p^2\ ,$$

where k and k' are, respectively, the four-momenta of the initial and final positrons, P is the initial proton four-momentum, y is the fraction of the energy transferred to the proton in its rest frame, m_p is the proton mass and W is the $\gamma^* p$ centre-of-mass energy.

For the description of the diffractive process $ep \to eXp$, in addition to the invariant mass of the system X, M_X, two further variables are introduced:

$$x_{I\!P} = \frac{M_X^2 + Q^2}{W^2 + Q^2}, \quad \beta = \frac{Q^2}{Q^2 + M_X^2}.$$

In resolved Pomeron models, where the interaction is described as the exchange of a particle-like Pomeron, $x_{I\!P}$ is the fraction of the proton momentum carried by the Pomeron and β is the fraction of its momentum carried by the parton within it that is probed by the virtual photon.

4 Monte Carlo simulations

Three Monte Carlo (MC) models for the diffractive deep inelastic process $ep \to eXp$ have been considered in order to describe the diffractive hadronic final state.

The RAPGAP 2.08/06 MC generator [20] implements the Ingelman-Schlein factorisable model [5] for the Pomeron. The matrix elements for the $O(\alpha)$ process ($eq \to eq$) and for the $O(\alpha\alpha_S)$ processes ($eq \to eqg$, $eg \to eq\overline{q}$) are included. To avoid divergences in the matrix elements for the $O(\alpha\alpha_S)$ processes for massless quarks, a cut of $p_T^2 > 3$ GeV^2 was applied, where p_T is the transverse momentum of any of the outgoing partons with respect to the photon direction in the centre-of-mass frame of the hard scattering. The relative contribution of each component is determined by the quark and gluon densities within the Pomeron, which evolve according to the DGLAP equations. The H1 parameterisation [3] for the Pomeron parton densities with a 'hard gluon' carrying $\geq 80\%$ of the momentum at $Q_0^2 = 3$ GeV^2 was used. Two different RAPGAP MC samples were generated, in which the higher-order QCD corrections were treated in two different ways: either using the colour-dipole model (CDM) [21] as implemented in ARIADNE 4.08 [22] or using parton showers (PS) as implemented in LEPTO 6.1 [23]. The Lund string-fragmentation scheme [24] as implemented in JETSET 7.4 [25] was used for hadronisation. First-order electroweak corrections are taken into account via the HERACLES 4.6 program [26].

The RIDI 2.0 MC generator [27] implements the diffractive dissociation of the virtual photon into $q\overline{q}$ and $q\overline{q}g$ final states following the approach of Ryskin [7], in the framework of the leading logarithmic approximation of pQCD. Contributions from transversely and longitudinally polarised photons are included. The predicted cross section is proportional to the square of the gluon momentum density in the proton. The CTEQ4M parameterisation [28] for the parton densities was used. Final-state parton showers and fragmentation were implemented using JETSET 7.4. First-order radiative corrections were also included.

The SATRAP MC generator [29] is based on the Golec-Biernat and Wüsthoff model [30]. In this model, the diffractive cross section is expressed as the convolution of the photon wave-function, calculated for $q\overline{q}$ and $q\overline{q}g$ colour dipoles and including the contributions of both transversely and longitudinally polarised photons, with the dipole cross section for scattering on the proton. The parameters of the model were tuned to describe the total $\gamma^* p$ cross section as measured at HERA. Final-state parton showers and fragmentation were simulated via JETSET 7.4. First-order radiative corrections were taken into account via the HERACLES 4.6 program.

During the course of this analysis, it became clear that neither RIDI nor SATRAP gave a reasonable description of the data. As discussed in Section 8, this was traced to inadequacies in the implementation of the modelling of higher-order QCD processes in these models. Most notably, no initial-state parton cascades were included, and the final-state QCD radiation from the gluon in the dominant $q\overline{q}g$ contribution was suppressed. A new implementation of higher-order QCD processes in SATRAP was carried out [31, 32], in which the CDM approach was implemented in a similar fashion to that in RAPGAP. This model is referred to as SATRAP-CDM.

Processes where the proton dissociates into a system N, $ep \to eXN$, were generated using the EPSOFT 2.0 MC generator [33]. This simulates events based on the triple-Regge formalism [34] and an M_N distribution as measured for diffractive dissociation in pp scattering. Samples with different parameters for the simulation of the system N were considered.

Non-diffractive DIS background was generated including first-order QED radiative corrections using LEPTO 6.5 interfaced to HERACLES 4.5 via DJANGOH 1.1 [35]. The CTEQ4M set of proton parton densities was used. The colour-dipole model was used to simulate parton cascades and fragmentation was performed using JETSET 7.4.

The RAPGAP-CDM model provides a good description of most of the measured distributions and was used to study the accuracy of the kinematic variables and jet reconstruction, the efficiency for selecting events and the corrections for detector and resolution effects. The detector simulation was based on the GEANT 3.13 program [36].

5 Event reconstruction and selection

The variables Q^2 and W were determined from the information of the scattered positron. The hadronic final-state system, X, resulting from the dissociation of the virtual photon, was reconstructed using "energy flow objects", hereafter denoted as EFOs [37], assumed to have the mass of the pion. These EFOs combine information from charged tracks, as measured in the CTD, and energy clusters measured in the CAL and FPC. In the kinematic region considered in this analysis, the invariant mass M_X was reconstructed on average with a systematic shift of -14% and a relative resolution of 10%, while the hadronic three-vector was reconstructed with a resolution of about 1 GeV for the X and Y components and ~ 2 GeV for the Z component. The four-momentum of the virtual photon, q, was determined with no significant bias and with a relative resolution of about 10% for the X and Y components and $\sim 7\%$ for the Z and energy components.

The triggering and online event selections were similar to those used for the ZEUS measurement of the structure function F_2 [37]. The offline selection criteria, applied to select diffractive DIS events, required:

- a scattered positron candidate (identified [38] via its pattern of energy deposition in the calorimeter) with energy, E'_e, greater than 10 GeV and $y < 0.95$. For an incoming positron

of energy E_e, y was estimated from the energy and the polar angle, θ'_e, of the scattered positron by:

$$y = 1 - \frac{E'_e}{2E_e}(1 - \cos\theta'_{\rm e}) \ .$$

The impact position of the scattered positron in the RCAL was required to be outside a box of 26×20 cm^2 around the beam pipe to ensure a fully contained positron candidate. In addition, candidates within the CTD acceptance region, but without a matched charged track reconstructed in the CTD, were rejected;

- $40 < \delta < 70$ GeV, where $\delta = \sum_i E_i(1 - \cos\theta_{\rm i})$ and the sum runs over all calorimeter cells, i.e. including those belonging to the scattered positron. This cut, together with the previous requirements on the positron candidate, eliminated background from photoproduction events and beam-gas interactions producing fake scattered positrons;
- a reconstructed vertex with $|Z| < 50$ cm and at least two associated tracks;
- the presence of a large rapidity gap in the outgoing proton direction, to select diffractive events. Events with $\eta^{\rm max} < 3.0$ were selected, where $\eta^{\rm max}$ is the pseudorapidity of the most-forward cluster with energy above 400 MeV, as measured in the CAL and FPC;
- at least three reconstructed EFOs in the hadronic final state to ensure that the event plane could be determined.

The measurements were limited to the following kinematic range:

- $5 < Q^2 < 100$ GeV^2;
- $200 < W < 250$ GeV;
- $23 < M_X < 40$ GeV, where M_X was corrected for energy losses (see Section 6.1);
- $x_{I\!P} < 0.025$.

In this region, the diffractive hadronic final state X is well contained in the central detector, thus minimising energy losses through the forward and rear beam-pipe holes. A good separation of the diffractive signal from the non-diffractive background was achieved: after the $\eta^{\rm max}$ requirement, the background was typically around 3% and at most 10%, as estimated from MC studies. After all cuts, 7175 events remained.

6 Three-jet search

A search for jets was performed in the centre-of-mass system of the observed hadronic final state, X, using the exclusive k_T-algorithm [39]. All EFOs in the event were used as input to the jet-finding procedure. For each pair of particles (EFOs) i and j in an event, the quantity

$$y_{ij} = \frac{2 \cdot \min(E_i^2, E_j^2)(1 - cos\theta_{ij})}{M_X^2}$$

was computed, where E_i is the energy of the i^{th} particle and θ_{ij} is the angle between particles i and j. The pair of particles with the smallest value of y_{ij} was replaced by a *pseudo-particle*

or cluster. The four-momentum of the cluster was determined using the "E-recombination scheme":

$$E^{\rm cluster} = E_i + E_j, \qquad P_k^{\rm cluster} = P_k^i + P_k^j \quad (k = X, Y, Z).$$

This clustering procedure was repeated until all y_{ij} values exceeded a given threshold, $y_{\rm cut}$, and all the remaining clusters were then labelled as jets. For this recombination scheme, the jets become massive and the total invariant mass, M_X, coincides with the invariant mass of the three-jet system. As applied in the centre-of-mass system, this algorithm produces at least two jets in every event. The same jet search procedure was applied to the final-state hadrons for simulated events.

Figure 1 shows the measured $n_{\rm jet}$ fractions for $n_{\rm jet} = 2, 3$ and > 3 as a function of the jet resolution parameter, $y_{\rm cut}$, in the region $0.01 < y_{\rm cut} < 0.1$. The rate of three-jet production varies from 47% at $y_{\rm cut} = 0.01$ to 8% at $y_{\rm cut} = 0.1$. The measured jet fractions were compared with diffractive MC models. All the models show trends similar to the data but only SATRAP-CDM provides a good description of the measurements. The predicted $n_{\rm jet}$ fractions are sensitive to the particular implementation of higher-order QCD corrections and hadronisation processes in each MC model. The differences observed between the predicted jet fractions from RAPGAP-CDM and RAPGAP-PS for $y_{\rm cut} \lesssim 0.03$ indicate where the dependence on the model used for the simulation of higher-order QCD contributions starts to be sizeable.

Good parton-hadron correlation in three-jet production was observed in the MC simulation for $M_X > 20$ GeV. In this mass range, values for $y_{\rm cut}$ around 0.05 gave the smallest hadronisation corrections. The parton-hadron jet correlation was studied using a MC sample with three jets found in the final state at both parton and hadron levels. The angular distance between each parton and the corresponding jet of hadrons was such that the partons were always well contained within the size of the hadron jets, which have a typical angular radius larger than 0.5 radians.

6.1 Jet reconstruction and selection

The reconstruction of the jet variables was studied using MC events with three jets at both hadron and detector levels. Matched pairs of jets were selected and used to study the jet reconstruction in the detector. The characteristics of the reconstructed jet quantities were found to be as follows:

- the polar angle of the jet, $\theta^*_{\rm jet}$, defined with respect to the $\gamma^* I\!P$ axis[3], was reconstructed with no significant systematic bias and a resolution of $\sim 6^\circ$ and $\sim 8^\circ$ for the two most energetic jets and the least energetic jet in the event, respectively;

- the measured invariant mass, M_X, and jet energies, $E^*_{\rm jet}$, were corrected for the energy loss by a common factor of 1.14, determined from MC studies. In the kinematic range considered, the jet energy was reconstructed with a typical resolution of 10% and the jet energy correction was independent of the jet direction;

- the transverse momentum of the jets, $P^*_{T,{\rm jet}}$, measured with respect to the $\gamma^* I\!P$ axis, was reconstructed without significant bias and with a resolution of 0.7 GeV;

[3]In the centre-of-mass system, the Pomeron defines the positive Z direction.

- the jet pseudorapidity, $\eta^{\rm jet}_{\rm lab}$, measured in the laboratory frame (see below), was reconstructed without significant bias and with a resolution of 0.1 to 0.2 units.

In addition, it was checked that, in the M_X region considered and for a fixed value of $y_{\rm cut} = 0.05$, the jets, defined in the centre-of-mass frame, always had energy significantly above the noise level in the CAL. The jet energies in the laboratory frame, $E^{\rm jet}_{\rm lab}$, computed by boosting the jet four-momenta in the centre-of-mass system back to the laboratory frame, were typically above 4 GeV, thus ensuring a well understood jet-energy reconstruction for all jets.

The sample of three-jet final states was defined by using a fixed $y_{\rm cut} = 0.05$ and the jets were required to be in the range $|\eta^{\rm jet}_{\rm lab}| < 2.3$. The variable $\eta^{\rm jet}_{\rm lab}$ was computed in the same way as $E^{\rm jet}_{\rm lab}$. The effect of the inclusion of jet masses in the determination of $\eta^{\rm jet}_{\rm lab}$ was found to be negligible. This procedure selected events with jets reconstructed in the central part of the detector, which are not affected by the $\eta^{\rm max}$ cut applied in the forward region and for which a good correlation between the jet before and after detector effects was preserved. After the $\eta^{\rm jet}_{\rm lab}$ cut, a final sample of 891 events with exactly three identified jets was obtained.

6.2 Three-jet topology variables

Neglecting jet mass, the topology of a three-jet final state can be described using the fractional-momentum variables

$$x_i = \frac{2 \cdot |\mathbf{P}^{\rm jet}_i|}{\sum_j |\mathbf{P}^{\rm jet}_j|}, \qquad |\mathbf{P}^{\rm jet}_i| = \sqrt{(P^{\rm jet}_{i,X})^2 + (P^{\rm jet}_{i,Y})^2 + (P^{\rm jet}_{i,Z})^2}\ , \tag{1}$$

where $\mathbf{P}^{\rm jet}_i$ $(i = 1 - 3)$ denotes the $i^{\rm th}$ jet three-momentum, determined in the centre-of-mass frame, and by construction $x_1 + x_2 + x_3 = 2$. The jets were sorted according to their momenta in such a way that

$$x_1 \geq x_2 \geq x_3\ .$$

Two of the x_i variables in Eq. (1) are sufficient to describe the jet topology in the final state. Following the studies of three-jet production in e^+e^- collisions at PETRA [40, 41], these quantities were chosen to be x_1 and $\xi = (x_2 - x_3)/x_1$, as suggested by Ellis and Karliner [42].

6.3 Jet-shape reconstruction

The internal structure of the jets was studied in terms of the differential jet shape, defined in the centre-of-mass system as the average of the fraction of the jet energy which lies inside an annulus of inner angular distance $\varphi - \delta\varphi/2$ and outer angular distance $\varphi + \delta\varphi/2$ from the jet axis. EFOs were used to reconstruct the jet shape defined as

$$\rho^{\rm EFOs}(\varphi) = \frac{1}{\delta\varphi\ N_{\rm jets}} \sum_{\rm jets} \frac{\Delta E^*_{\rm jet}(\varphi \pm \delta\varphi/2)}{E^*_{\rm jet}}\ ,$$

where $\Delta E^*_{\rm jet}(\varphi \pm \delta\varphi/2)$ denotes the sum of the energies of the EFOs belonging to a given jet whose angular distance to the jet axis is within the range $(\varphi - \delta\varphi/2, \varphi + \delta\varphi/2)$ with $\delta\varphi = 0.2$ radians; $N_{\rm jets}$ is the number of jets. For MC events, the same jet-shape definition as used above for the EFOs was applied to the final-state hadrons.

7 Unfolding and systematic studies

The measured distributions were corrected bin-by-bin for acceptance and migrations using RAPGAP-CDM. The measurement was carried out in the region $5 < Q^2 < 100$ GeV^2, $200 < W < 250$ GeV, $23 < M_X < 40$ GeV and $x_{I\!P} < 0.025$, for diffractive events with $\eta^{\rm max}_{\rm hadron} < 3.0$ and $|\eta^{\rm jet}_{\rm lab}|_{\rm hadron} < 2.3$, where $\eta^{\rm max}_{\rm hadron}$ is the pseudorapidity of the most-forward final-state hadron with energy above 400 MeV. The measurements presented here thus cover a very restricted phase-space region. According to RAPGAP, in the kinematic region considered, less than 10% of all diffractive events have $\eta^{\rm max}_{\rm hadron} < 3.0$ and three jets in the final state with $|\eta^{\rm jet}_{\rm lab}|_{\rm hadron} < 2.3$. The fraction of three-jet events selected by the $\eta^{\rm max}_{\rm hadron} < 3.0$ and $|\eta^{\rm jet}_{\rm lab}|_{\rm hadron} < 2.3$ requirements was estimated using RAPGAP to be of the order of 30%.

A detailed study of the main sources contributing to the systematic uncertainties of the measurements was performed [31]. The different contributions are listed below, with a typical value quoted for each:

- the uncertainty in the hadronic final-state energy scale was taken into account by varying the CAL (FPC) energy by $\pm 3\%$ ($\pm 10\%$) in the MC, after removing the energy deposits belonging to the scattered positron. This introduced an uncertainty in the measured distributions of about 5%;

- the selected window in the reconstructed M_X was varied by $\pm 10\%$, both in data and simulated events, according to the estimated resolution in the reconstruction of this quantity. The measured cross sections varied by 5%;

- the uncertainty in the positron energy scale was included by varying the positron energy by $\pm 2\%$ in the MC. The effect on the $\eta^*_{\rm jet}$ and $P^*_{T,{\rm jet}}$ distributions (see Section 8) was typically below 3%;

- the box cut applied to the position of the scattered positron in the RCAL was varied by ± 5 mm (both in data and simulated events) to account for the uncertainty in simulating the measured positron position. The effect was typically below 1%;

- the selected range in the reconstructed jet pseudorapidity in the laboratory frame, $|\eta^{\rm jet}_{\rm lab}| < 2.3$, (see Section 6.1) was varied by 0.2 units around the nominal value, both in data and MC simulation, according to the estimated resolution in the reconstruction of the jet direction. This introduced an uncertainty on the measured cross sections of about 2%;

- the measured distributions were corrected to the hadron level using RAPGAP-PS instead of RAPGAP-CDM to account for the uncertainty in the simulation of higher-order QCD processes in the MC model. The effect varied between 5% and 10% and was the dominant systematic uncertainty.

The final systematic uncertainty was computed by adding the different contributions in quadrature. The contribution from proton-dissociative processes, $ep \to eXN$, with $M_N \leq 3$ GeV, where the system N escaped through the forward beam hole in the FPC, was estimated using EPSOFT to be $(16 \pm 5)\%$ and was subtracted. The overall normalisation uncertainty of 5.4% in the measured cross sections, coming from the uncertainty on the proton-dissociative contribution and the 2% error in the luminosity determination, is not included in the figures.

8 Results

Multi-jet production in the centre-of-mass system of the hadronic final state, X, is presented in the kinematic region defined in Section 7 using the exclusive k_T-algorithm with $y_{\rm cut} = 0.05$. The measurements[4] were corrected for electroweak radiative effects to the Born level.

8.1 Three-jet topology

The topology of the three-jet final state was studied using x_i, the fractional-momentum variables (see Section 6.2). Figure 2(a) shows the distribution of the three-jet sample in the $(\xi,\ x_1)$ plane. As indicated in the figure, different regions in the plane correspond to different three-jet topologies. All configurations are present, including those for which the three jets have similar energies. The distribution of the events shows that, for the given $y_{\rm cut}$, the favoured three-jet topologies are those for which one leading jet carries approximately twice the energy of either of the other two jets ($\xi \simeq 0.1, x_1 \simeq 0.9$). The normalised differential cross sections for three-jet production as a function of x_1 and ξ are presented in Figs. 2(b) and 2(c), compared to the MC predictions. The measured x_1 distribution has a peak structure with a maximum at $x_1 \simeq 0.9$, which is determined by the $y_{\rm cut}$ value used in defining jets since the position of the peak approximately corresponds to $1-2y_{\rm cut}$. The shapes of the measured cross sections are reproduced by all three MC models. This indicates that they provide a good description of the dynamics of the three-jet emission, which dictates the population of the $(\xi,\ x_1)$ plane.

The energy flow, as measured in the event plane defined by the two most-energetic jets in the event, was studied as a function of the azimuthal angle, ϕ^*. The origin of ϕ^* was defined to be along the direction of the most-energetic jet with positive ϕ^* increasing in the direction of the second most-energetic jet. The energy flow was measured by projecting the particle momenta onto the event plane and summing, in each ϕ^* bin, the particle energies. The sums were normalised by dividing by M_X. In Fig. 3, the normalised energy flow is presented for different regions of the $(\xi,\ x_1)$ plane. A clear three-jet structure is observed in all regions. The measurements are compared with the RAPGAP and SATRAP-CDM predictions. RAPGAP-CDM, RAPGAP-PS (not shown but similar to RAPGAP-CDM) and SATRAP-CDM all provide a very good description of the measured flows for all $(\xi,\ x_1)$ regions and ϕ^* ranges.

8.2 Cross section as a function of $\eta^*_{\rm jet}$

Figure 4(a,b) shows the differential cross section as a function of the jet pseudorapidity, $d\sigma/d\eta^*_{\rm jet}$, measured with respect to the $\gamma^* I\!P$ axis. All jets in each event were included. The total cross section for three-jet production, obtained by integrating the differential measurement, is:

$$\sigma^{\rm 3jets} = \frac{1}{3} \cdot \int \frac{d\sigma}{d\eta^*_{\rm jet}}\, d\eta^*_{\rm jet} = 14.1 \pm 0.5({\rm stat.})^{+1.3}_{-1.1}({\rm syst.})\ {\rm pb}.$$

For this measurement, the overall normalisation uncertainty of 5.4% (see Section 7) is combined in quadrature in the quoted total systematic uncertainty. The measured cross section corresponds to $32.2\% \pm 0.9\%({\rm stat.})^{+1.3}_{-1.6}\%({\rm syst.})$ of the diffractive cross section for two or more

[4]The measurements are tabulated in Tables 1 - 7.

jets. This rate is consistent with being independent of Q^2 and M_X.

Figure 4(a) shows the measured differential cross section compared to the RAPGAP-CDM and RAPGAP-PS predictions. Both implementations of RAPGAP provide a good description of the shape of the cross section but underestimate it by about 20%. The observed deficit in the absolute normalisation predicted by RAPGAP may be attributed to the absence of next-to-leading-order terms in the computed matrix elements, which are only approximated via parton cascades.

In Fig. 4(b) the measured differential cross section is compared to the SATRAP, SATRAP-CDM and RIDI predictions. For the latter, the contribution from the hadron jet associated with the gluon from the $q\overline{q}g$ final state is shown separately. The SATRAP and RIDI predictions are found to be more than a factor of two below the measured cross sections and show a double-peak structure not observed in the data. This tendency is particularly pronounced in RIDI. This reflects the presence of dominant topologies in these models in which the jet in the Pomeron direction is emitted almost collinear to the $\gamma^* I\!P$ axis and for which the second and third jets are found in the photon hemisphere. The observed shape of the SATRAP and RIDI predictions is a consequence of the inadequacies of the implementation of the modelling of higher-order QCD processes in these MC models as discussed in Section 4. SATRAP-CDM describes the shape of the measured distribution but also underestimates the normalisation by about 20%, which, as for RAPGAP, may be attributed to the absence of next-to-leading-order and some leading-order terms in the computed matrix elements.

8.3 $P^*_{T,\mathrm{jet}}$ distribution for the most-forward jet

The differential cross section as a function of the jet transverse momentum, $P^*_{T,\mathrm{jet}}$, measured with respect to the $\gamma^* I\!P$ axis for the most-forward jet is presented in Fig. 4(c,d). The measurement was performed in the region $P^*_{T,\mathrm{jet}} > 1$ GeV, where a good parton jet-hadron jet correlation is preserved, and for which the measurement is well defined, given the estimated resolution in the reconstruction of $P^*_{T,\mathrm{jet}}$ in the detector (see Section 6). The measured cross section is dominated by configurations with $P^*_{T,\mathrm{jet}}$ below 3 GeV but contains a long tail towards larger $P^*_{T,\mathrm{jet}}$ values, reflecting the presence of contributions from higher-order QCD processes.

Figure 4(c) shows the measured cross section compared to RAPGAP-CDM and RAPGAP-PS. The RAPGAP predictions underestimate the measured cross section and have a slightly different shape than the data. RAPGAP-CDM provides a better description of the data than RAPGAP-PS. The observed difference between these two predictions indicates the sensitivity of the $P^*_{T,\mathrm{jet}}$ distribution to the approach used for the simulation of higher-order QCD processes in the MC.

Figure 4(d) shows the measured $P^*_{T,\mathrm{jet}}$ distribution compared to the predictions from SATRAP, SATRAP-CDM and RIDI. The $P^*_{T,\mathrm{jet}}$ distribution predicted by SATRAP and RIDI is steeper than that of the data, indicating that, in these MC models, the large $P^*_{T,\mathrm{jet}}$ configurations are missing. The cross section in these models is dominated by configurations strongly aligned with respect to the $\gamma^* I\!P$ axis in the forward region. As already mentioned, this is most probably a consequence of the inadequacies of the implementation of the modelling of higher-order QCD processes in these models. In SATRAP-CDM, the shape and normalisation of the $P^*_{T,\mathrm{jet}}$ distri-

bution is in better agreement with the data.

In all models, the gluon in the $q\overline{q}g$ final state is emitted with very small transverse momentum with respect to the $\gamma^* I\!P$ axis. The contributions from higher-order QCD processes are expected to be important and to influence the kinematics of the corresponding hadron jet which, due to string effects, tends to have smaller pseudorapidity (larger transverse momentum) compared to the initial parton. Given the $|\eta^{\rm jet}_{\rm lab}|_{\rm hadron} < 2.3$ requirement applied in defining the measured cross sections, the absolute predictions from these models depend on an appropriate treatment of these higher-order QCD emissions and a proper description of the forward hadron-jet dynamics (as shown in Fig. 4(d)). This is particularly clear in the case of SATRAP, which fails to reproduce the three-jet data but provides a good description of inclusive diffractive DIS [29].

8.4 Jet shapes

The differential jet shapes, $\rho(\varphi)$, were measured for the most-forward and most-backward jet in three-jet events, where the forward region is defined by the Pomeron direction. The measurements were performed in the $\gamma^* I\!P$ centre-of-mass frame for jets with energy, $E^*_{\rm jet}$, above 9 GeV. This requirement removes the contributions from the least-energetic jet in the event which, in the M_X-range considered and for the given $y_{\rm cut}$, has energy below this threshold and for which hadronisation effects on the jet shape are expected to be important. Figure 5 shows the measured jet shapes compared with the RAPGAP-CDM predictions (the SATRAP-CDM predictions, not shown, are almost identical). The jet in the Pomeron direction is broader than the jet in the photon direction. These measurements are described by models in which a gluon populates the Pomeron hemisphere and a quark is found in the photon direction. The energy distribution of the two jets is similar, indicating that the observed difference in the measured jet shapes can be ascribed to the different nature of the initial partons. Moreover, the difference between the jet shapes in the Pomeron and photon directions is qualitatively similar to that between quark- and gluon-initiated jets as measured in e^+e^- experiments [43]. This measurement therefore supports the validity of the picture where the three-body final state is dominated by a $q\overline{q}g$ configuration with the gluon preferentially emitted in the Pomeron direction.

9 Summary and conclusions

Multi-jet production has been studied in the kinematic region $5 < Q^2 < 100$ GeV^2, $200 < W < 250$ GeV, $23 < M_X < 40$ GeV and $x_{I\!P} < 0.025$, for diffractive events with $\eta^{\rm max}_{\rm hadron} < 3.0$ and $|\eta^{\rm jet}_{\rm lab}|_{\rm hadron} < 2.3$. A study of three-jet production, using the exclusive k_T-algorithm with $y_{\rm cut} = 0.05$ in the centre-of-mass system of the hadronic final state, has been presented. The rate of three-jet production has been measured to be $32.2\% \pm 0.9\%({\rm stat.})^{+1.3}_{-1.6}\%({\rm syst.})$ of the diffractive jet cross section, and is consistent with being independent of Q^2 and M_X. The topologies of the three-jet final states have been studied in terms of the jet fractional-momentum variables ξ and x_1; all possible topologies have been observed. The distribution of the events in the $(\xi,\ x_1)$ plane shows that, for a given $y_{\rm cut}$, the favoured topologies are those for which one leading jet carries approximately twice the energy of either of the other two jets ($\xi \simeq 0.1, x_1 \simeq 0.9$). Differential cross sections for three-jet production have been measured as a function of the jet pseudorapidity, $\eta^*_{\rm jet}$, and jet transverse momentum, $P^*_{T,{\rm jet}}$, with respect to the $\gamma^* I\!P$ axis. The total cross section for three-jet production, determined by integrating the $\eta^*_{\rm jet}$ distribution,

is $\sigma^{\rm 3jets} = 14.1 \pm 0.5({\rm stat.})^{+1.3}_{-1.1}({\rm syst.})$ pb. The $P^*_{T,{\rm jet}}$ distribution for the most-forward jet is dominated by configurations with $P^*_{T,{\rm jet}}$ below 3 GeV but exhibits a long tail towards larger values, reflecting the presence of higher-order QCD contributions. The differential jet shapes, $\rho(\varphi)$, of the two most-energetic jets in three-jet events have been measured. The jet in the Pomeron direction is broader and consistent with the shape of gluon-initiated jets as predicted by diffractive MC models.

The data are broadly consistent with models in which the hadronic final-state is dominated by a $q\overline{q}g$ system with the gluon preferentially emitted in the Pomeron direction. Such configurations are predicted both by resolved Pomeron models (as implemented in RAPGAP) with a Pomeron dominated by gluons, and by models where the virtual photon dissociates in a $q\overline{q}g$ system which interacts with the proton via the exchange of a gluon ladder (as implemented in SATRAP and RIDI). RAPGAP provides a reasonable description of the measured distributions, although it underestimates the measured cross section by about 20%. This deficit may be attributed to the absence of next-to-leading-order corrections, which are only included approximately via parton cascades. The predictions from SATRAP and RIDI fail to describe the shape and normalisation of the $\eta^*_{\rm jet}$ and $P^*_{T,{\rm jet}}$ distributions. However, it has been shown that an improved implementation of the modelling of higher-order QCD processes in SATRAP-CDM gives reasonable agreement with the data. Thus, the study of three jets in diffraction constitutes a very sensitive method to investigate the dynamics of diffractive deep inelastic scattering.

Acknowledgements

The strong support and encouragement of the DESY Directorate have been invaluable. The experiment was made possible by the inventiveness and the diligent efforts of the HERA machine group. The design, construction and installation of the ZEUS detector have been made possible by the ingenuity and dedicated efforts of many people from inside DESY and from the home institutes who are not listed as authors. Their contributions are acknowledged with great appreciation. We would like to thank the staff support from the various Institutes which collaborated in the construction of the FPC and in the setup of the test systems, in particular J. Hauschildt and K. Löffler (DESY), L. Hervás (CERN), R. Feller, E. Möller and H. Prause (I. Inst. for Exp. Phys., Hamburg), A. Maniatis (II. Inst. for Exp. Phys., Hamburg), and the members of the mechanical workshop of the Faculty of Physics from Freiburg University.

References

[1] ZEUS Collaboration, M. Derrick et al., Nucl. Phys. B 315 (1993) 481;
H1 Collaboration, T. Ahmed et al., Nucl. Phys. B 429 (1994) 477.

[2] A. Donnachie and P.V. Landshoff, Phys. Lett. B 296 (1992) 227.

[3] H1 Collaboration, C. Adloff et al., Z. Phys. C 76 (1997) 613.

[4] ZEUS Collaboration, M. Derrick et al., Phys. Lett. B 356 (1995) 129;
ZEUS Collaboration, J. Breitweg et al., Eur. Phys. J. C 5 (1998) 41.

[5] G. Ingelman and P. Schlein, Phys. Lett. B 152 (1985) 256.

[6] See e.g. *Proceedings of the Workshop on Future Physics at HERA*, G. Ingelman, A. De Roeck and R. Klanner (eds.), Vol. 2, DESY, Hamburg, (1996), and references therein.

[7] M.G. Ryskin, Sov. J. Nucl. Phy. 52 (1990) 529.

[8] N.N. Nikolaev and B.G. Zakharov, Z. Phys. C 5 (1992) 331;
M. Wüsthoff, Phys. Rev. D 56 (1997) 4311;
W. Buchmüller, A. Hebecker and M.F. McDermott, Nucl. Phys. B 487 (1997) 283;
J. Bartels et al., Eur. Phys. J. C 7 (1999) 443.

[9] ZEUS Collaboration, J. Breitweg et al., Eur. Phys. J. C 6 (1999) 43.

[10] H1 Collaboration, S. Aid et al., Z. Phys. C 70 (1996) 609;
H1 Collaboration, C. Adloff et al., Phys. Lett. B 428 (1998) 206;
H1 Collaboration, C. Adloff et al., Eur. Phys. J. C 1 (1998) 495;
H1 Collaboration, C. Adloff et al., Eur. Phys. J. C 6 (1999) 421;
H1 Collaboration, C. Adloff et al., Eur. Phys. J. C 20 (2001) 29.

[11] ZEUS Collaboration, M. Derrick et al., Phys. Lett. B 332 (1994) 228;
ZEUS Collaboration, M. Derrick et al., Z. Phys. C 67 (1995) 227;
ZEUS Collaboration, J. Breitweg et al., Phys. Lett. B 421 (1998) 368.

[12] For a review of PETRA results, see e.g.:
S.L. Wu, Phys. Rep. 107 (1984) 59;
B. Naroska, Phys. Rep. 148 (1987) 67.

[13] ZEUS Collaboration, M. Derrick et al., Phys. Lett. B 293 (1992) 465;
ZEUS Collaboration, M. Derrick et al., Z. Phys. C 63 (1994) 391.

[14] ZEUS Collaboration, U. Holm (ed.), *The ZEUS Detector*, Status Report (unpublished), DESY, 1993, available on
`http://www-zeus.desy.de/bluebook/bluebook.html`.

[15] M. Derrick et al., Nucl. Instr. and Meth. A 309 (1991) 77;
A. Andresen et al., Nucl. Instr. and Meth. A 309 (1991) 101;
A. Caldwell et al., Nucl. Instr. and Meth. A 321 (1992) 356;
A. Bernstein et al., Nucl. Instr. and Meth. A 336 (1993) 23.

[16] N. Harnew et al., Nucl. Instr. and Meth. A 279 (1989) 290;
B. Foster et al., Nucl. Phys. Proc. Suppl. B 32 (1993) 181;
B. Foster et al., Nucl. Instr. and Meth. A 338 (1994) 254.

[17] A. Bamberger et al., Nucl. Instr. and Meth. A 450 (2000) 235.

[18] A. Bamberger et al., Nucl. Instr. and Meth. A 401 (1997) 63.

[19] J. Andruszków et al., DESY 01-041 (2001);
ZEUS Collaboration, M. Derrick et al., Z. Phys. C 63 (1994) 391.

[20] RAPGAP (version 2.08/06), H. Jung, Comp. Phys. Comm. 86 (1995) 147.

[21] Y. Azimov et al., Phys. Lett. B 165 (1985) 147;
G. Gustafson, Phys. Lett. B 175 (1986) 453;
G. Gustafson and U. Petersson, Nucl. Phys. B 306 (1988) 746;
B. Andersson, G. Gustafson and L. Lönnblad, Z. Phys. C 43 (1989) 625.

[22] L. Lönnblad, Comp. Phys. Comm. 71 (1992) 15; Z. Phys. C 65 (1995) 285.

[23] G. Ingelman, A. Edin and J. Rathsman, Comp. Phys. Comm. 101 (1997) 108.

[24] B. Andersson et al., Phys. Rep. 97 (1983) 31.

[25] H.-U. Bengtsson and T. Sjöstrand, Comp. Phys. Comm. 46 (1987) 43;
T. Sjöstrand, Comp. Phys. Comm. 82 (1994) 74.

[26] K. Kwiatkowski, H. Spiesberger and H.-J. Möhring, Comp. Phys. Comm. 69 (1992) 155.

[27] RIDI (version 2.0), M.G. Ryskin and A. Solano, *Proceedings of the Workshop on Monte Carlo Generators for HERA Physics*, Hamburg, Germany, A.T. Doyle et al., (eds.), DESY (1999), p. 386.

[28] H.L. Lai et al., Phys. Rev. D 55 (1997) 1280.

[29] H. Kowalski, DESY 99-141 (1999).

[30] K. Golec-Biernat and M. Wüsthoff, Phys. Rev. D 59 (1999) 014017;
K. Golec-Biernat and M. Wüsthoff, Phys. Rev. D 60 (1999) 114023.

[31] T. Yamashita, Ph.D. Thesis, University of Tokyo (2001), in preparation.

[32] H. Jung and H. Kowalski, private communication.

[33] M. Kasprzak, Ph.D. Thesis, Warsaw University, DESY F35D-96-16 (1996).

[34] R.D. Field and G. Fox, Nucl. Phys. B 80 (1974) 367;
A.H. Mueller, Phys. Rev. D 2 (1970) 2963; Phys. Rev. D 4 (1971) 150.

[35] K. Charchuła, G.A. Schuler and H. Spiesberger, Comp. Phys. Comm. 81 (1994) 381.

[36] GEANT 3, R. Brun et al., Technical Report CERN-DD/EE/84-1 (1987).

[37] ZEUS Collaboration, M. Derrick et al., Z. Phys. C 72 (1996) 399.

[38] H. Abramowicz, A. Caldwell and R. Sinkus, Nucl. Inst. and Meth. A 365 (1995) 508.

[39] S. Catani et al., Phys. Lett. B 269 (1991) 432.

[40] JADE Collaboration, W. Bartel et al., Phys. Lett. B 91 (1980) 142.

[41] TASSO Collaboration, R. Brandelik et al., Phys. Lett. B 97 (1980) 453.

[42] J. Ellis and I. Karliner, Nucl. Phys. B 148 (1979) 141.

[43] OPAL Collaboration, G. Alexander et al., Z. Phys. C 69 (1996) 543.

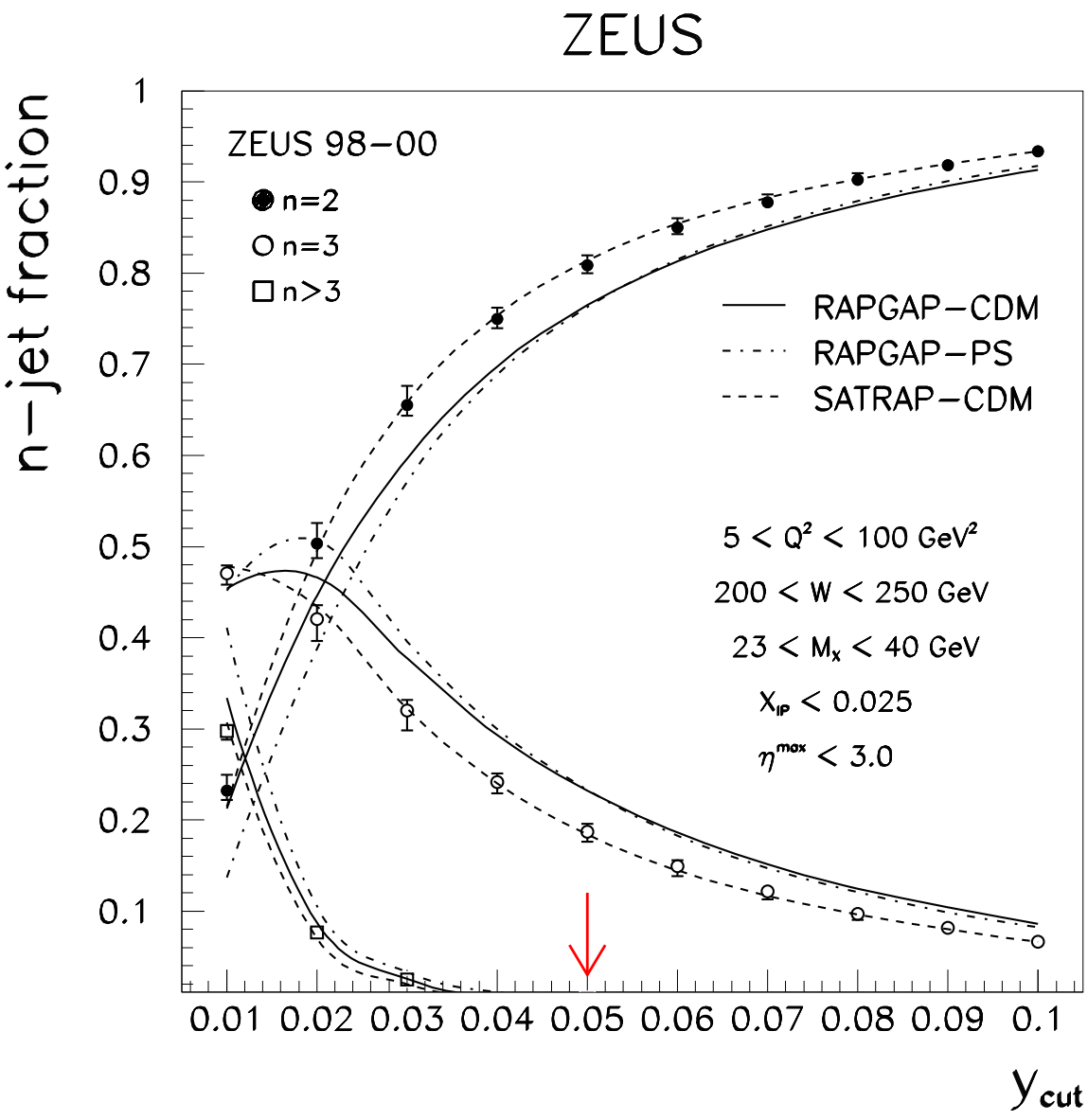

Figure 1: Measurement of the $n_{\rm jet}$-fraction, for $n_{\rm jet} = 2, 3$ and > 3, as a function of the exclusive k_T-jet resolution parameter, $y_{\rm cut}$. The MC expectations from RAPGAP-CDM (solid lines), RAPGAP-PS (dashed-dotted lines) and SATRAP-CDM (dashed lines) are shown. The vertical arrow at $y_{\rm cut} = 0.05$ indicates the value used in the subsequent analysis.

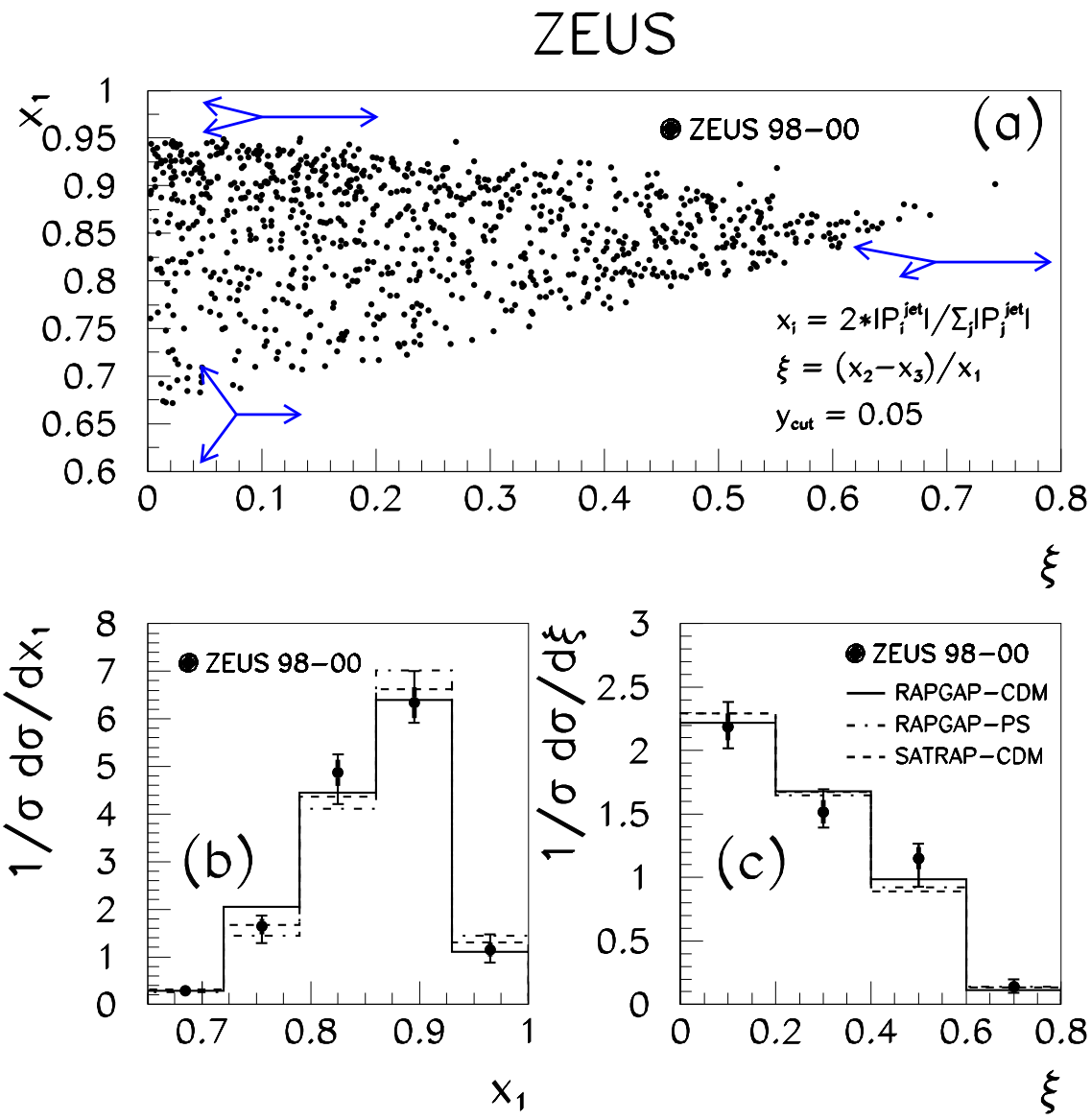

Figure 2: (a) Distribution of the three-jet sample in the (ξ, x_1) plane. The different topologies within the plane are indicated, where the length of the arrow represents the momentum of the jet as computed in the centre-of-mass frame. (b,c) Normalised differential cross sections as a function of x_1 and ξ in three-jet production. The thick error bars indicate the statistical uncertainties and the thin error bars indicate the statistical and systematic uncertainties combined in quadrature. The MC expectations from RAPGAP-CDM (solid line), RAPGAP-PS (dashed-dotted line) and SATRAP-CDM (dashed line) are shown.

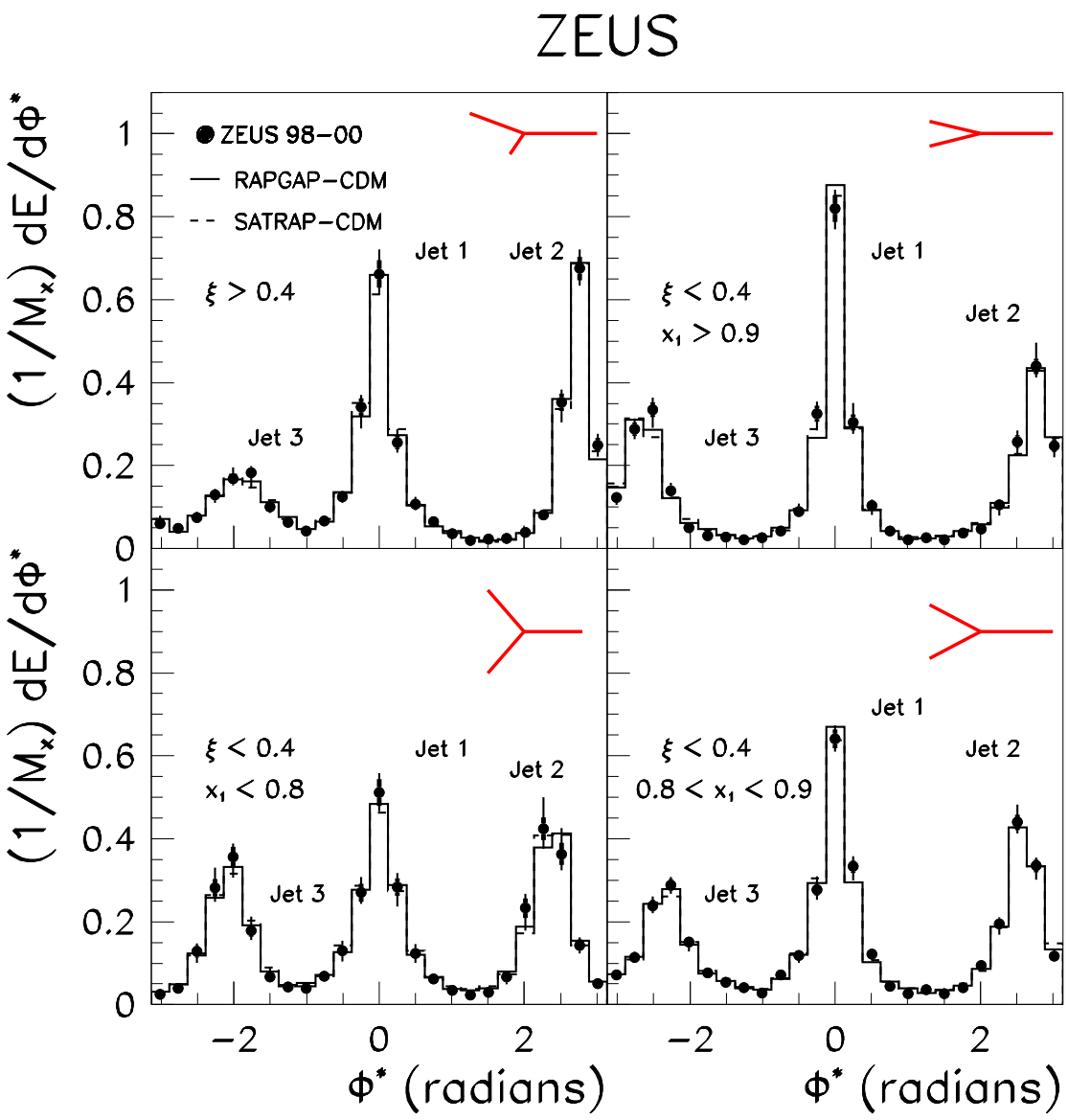

Figure 3: Energy-flow distribution in the three-jet plane, normalised to the total invariant mass, as a function of the azimuthal angle, ϕ^*, in the different regions of the (ξ, x_1) plane. The azimuthal angle is defined to run from the first to the second most-energetic jet in each event. The thick error bars indicate the statistical uncertainties and the thin error bars indicate the statistical and systematic uncertainties combined in quadrature. The MC expectations from RAPGAP-CDM (solid lines) and SATRAP-CDM (dashed lines) are shown. The characteristic topology of the three-jet configuration is indicated in the top right corner of each plot.

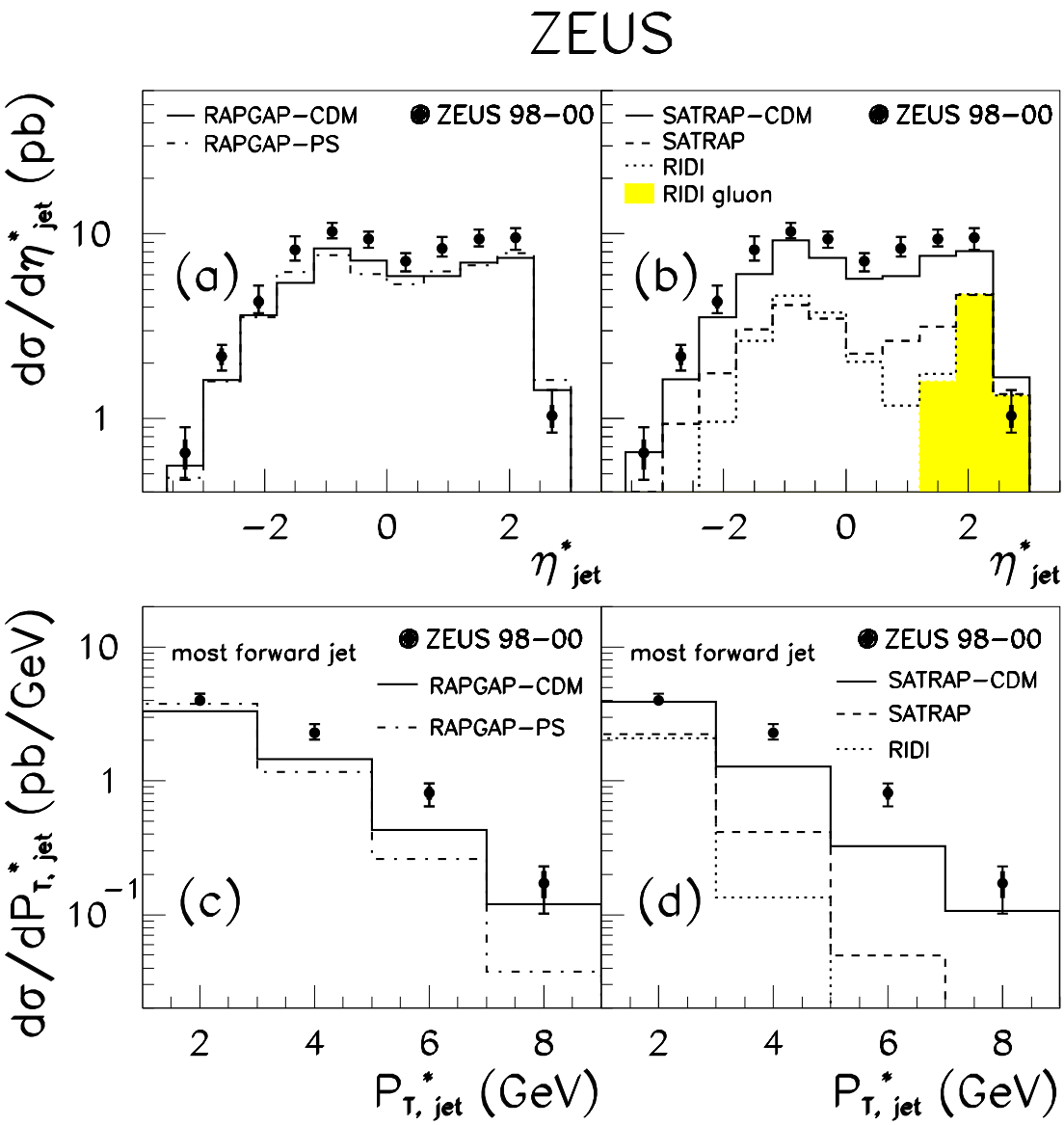

Figure 4: Differential cross section for three-jet production as a function of (a,b) the jet pseudorapidity, $d\sigma/d\eta^*_{\rm jet}$, of the three jets; (c,d) the jet transverse momentum, $P^*_{\rm T,jet}$, of the most-forward jet. The Pomeron direction defines the forward hemisphere. The thick error bars indicate the statistical uncertainties and the thin error bars indicate the statistical and systematic uncertainties combined in quadrature. The overall normalisation uncertainty of 5.4% was not included in the figures. The MC expectations are shown from (a,c) RAPGAP-CDM (solid line) and RAPGAP-PS (dashed-dotted line) and (b,d) SATRAP (dashed line), RIDI (dotted line) and SATRAP-CDM (solid line). For RIDI, the contribution from the gluon-initiated jet is shown separately in (b) (shaded area).

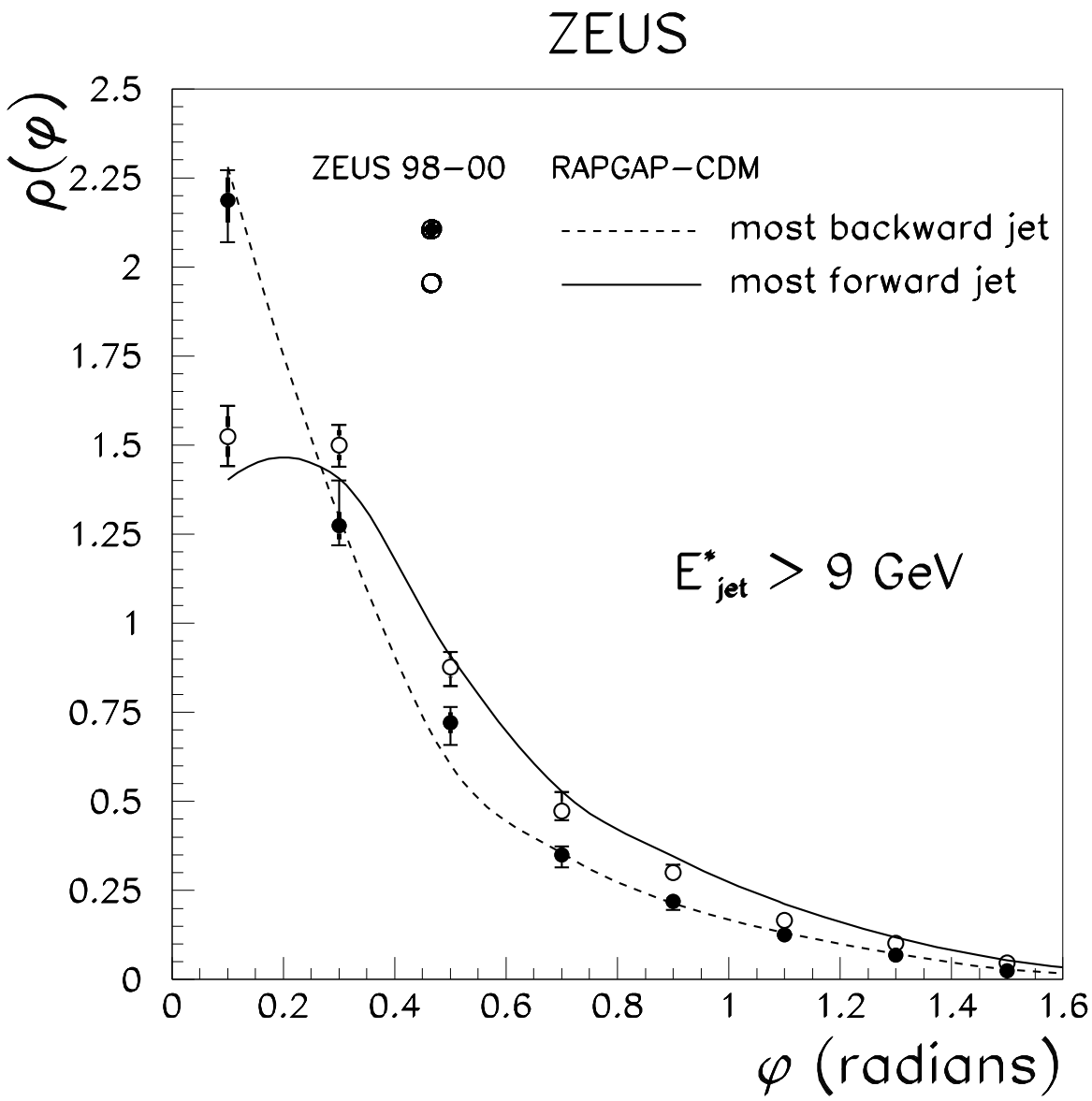

Figure 5: The differential jet shape, $\rho(\varphi)$, for the most-forward and most-backward jets with $E^*_{\rm jet} > 9$ GeV in three-jet events, where the Pomeron defines the forward direction. The thick error bars indicate the statistical uncertainties and the thin error bars indicate the statistical and systematic uncertainties combined in quadrature. The MC expectations from RAPGAP-CDM are shown.

$N_{\rm jet}$ fractions versus $y_{\rm cut}$						
	$N_{\rm jet}=2$		$N_{\rm jet}=3$		$N_{\rm jet}>3$	
$y_{\rm cut}$	rate	(stat. $\bigoplus$ syst.)	rate	(stat. $\bigoplus$ syst.)	rate	(stat. $\bigoplus$ syst.)
0.01	0.232	$^{+0.017}_{-0.010}$	0.471	$^{+0.008}_{-0.012}$	0.297	$^{+0.007}_{-0.009}$
0.02	0.503	$^{+0.023}_{-0.016}$	0.420	$^{+0.016}_{-0.024}$	0.077	$^{+0.004}_{-0.004}$
0.03	0.655	$^{+0.021}_{-0.012}$	0.320	$^{+0.011}_{-0.022}$	0.025	$^{+0.002}_{-0.002}$
0.04	0.750	$^{+0.012}_{-0.010}$	0.241	$^{+0.010}_{-0.012}$	0.009	$^{+0.001}_{-0.001}$
0.05	0.809	$^{+0.011}_{-0.009}$	0.187	$^{+0.009}_{-0.011}$	0.004	$^{+0.001}_{-0.001}$
0.06	0.850	$^{+0.011}_{-0.007}$	0.149	$^{+0.007}_{-0.011}$	0.001	$^{+0.001}_{-0.000}$
0.07	0.878	$^{+0.009}_{-0.006}$	0.122	$^{+0.006}_{-0.008}$	-	-
0.08	0.902	$^{+0.007}_{-0.006}$	0.097	$^{+0.005}_{-0.007}$	-	-
0.09	0.919	$^{+0.006}_{-0.004}$	0.081	$^{+0.004}_{-0.006}$	-	-
0.10	0.934	$^{+0.004}_{-0.004}$	0.066	$^{+0.004}_{-0.004}$	-	-

Table 1: Measurement of the $n_{\rm jet}$-fraction, for $n_{\rm jet}=2,3$ and >3, as a function of the exclusive k_T jet resolution parameter, $y_{\rm cut}$.

$\frac{1}{\sigma}\frac{d\sigma}{dx_1}$			
dx_1	$\frac{1}{\sigma}\frac{d\sigma}{dx_1}$	(stat.)	(stat. $\bigoplus$ syst.)
[0.650,0.720]	0.288	±0.056	$^{+0.098}_{-0.091}$
[0.720,0.790]	1.639	±0.162	$^{+0.226}_{-0.345}$
[0.790,0.860]	4.869	±0.277	$^{+0.387}_{-0.656}$
[0.860,0.930]	6.339	±0.319	$^{+0.668}_{-0.428}$
[0.930,1.000]	1.150	±0.150	$^{+0.319}_{-0.266}$

Table 2: Normalised differential cross section as a function of x_1.

$\frac{1}{\sigma}\frac{d\sigma}{d\xi}$			
$d\xi$	$\frac{1}{\sigma}\frac{d\sigma}{d\xi}$	(stat.)	(stat. $\bigoplus$ syst.)
[0.0,0.2]	2.189	±0.106	$^{+0.196}_{-0.169}$
[0.2,0.4]	1.516	±0.093	$^{+0.179}_{-0.123}$
[0.4,0.6]	1.153	±0.086	$^{+0.114}_{-0.225}$
[0.6,0.8]	0.142	±0.033	$^{+0.057}_{-0.051}$

Table 3: Normalised differential cross section as a function of ξ.

$\frac{1}{M_X}\frac{dE}{d\phi^*}$								
	$\xi > 0.4$		$\xi < 0.4,\ x_1 > 0.9$		$\xi < 0.4,\ x_1 < 0.8$		$\xi < 0.4,\ 0.8 < x_1 < 0.9$	
$\overline{\phi^*}$ (rad.)	$\frac{1}{M_X}\frac{dE}{d\phi^*}$	(stat. $\bigoplus$ syst.)	$\frac{1}{M_X}\frac{dE}{d\phi^*}$	(stat. $\bigoplus$ syst.)	$\frac{1}{M_X}\frac{dE}{d\phi^*}$	(stat. $\bigoplus$ syst.)	$\frac{1}{M_X}\frac{dE}{d\phi^*}$	(stat. $\bigoplus$ syst.)
-3.016	0.061	$^{+0.019}_{-0.008}$	0.122	$^{+0.014}_{-0.017}$	0.024	$^{+0.006}_{-0.005}$	0.072	$^{+0.008}_{-0.012}$
-2.765	0.049	$^{+0.009}_{-0.011}$	0.288	$^{+0.026}_{-0.024}$	0.040	$^{+0.007}_{-0.010}$	0.114	$^{+0.015}_{-0.011}$
-2.513	0.075	$^{+0.013}_{-0.012}$	0.335	$^{+0.029}_{-0.043}$	0.129	$^{+0.019}_{-0.028}$	0.239	$^{+0.023}_{-0.018}$
-2.262	0.130	$^{+0.014}_{-0.020}$	0.139	$^{+0.020}_{-0.014}$	0.282	$^{+0.048}_{-0.033}$	0.289	$^{+0.020}_{-0.022}$
-2.011	0.168	$^{+0.028}_{-0.015}$	0.050	$^{+0.010}_{-0.007}$	0.356	$^{+0.034}_{-0.049}$	0.151	$^{+0.012}_{-0.023}$
-1.759	0.182	$^{+0.016}_{-0.036}$	0.031	$^{+0.005}_{-0.006}$	0.179	$^{+0.033}_{-0.023}$	0.077	$^{+0.010}_{-0.008}$
-1.508	0.100	$^{+0.016}_{-0.014}$	0.027	$^{+0.007}_{-0.006}$	0.068	$^{+0.020}_{-0.013}$	0.054	$^{+0.008}_{-0.009}$
-1.257	0.063	$^{+0.013}_{-0.012}$	0.021	$^{+0.005}_{-0.007}$	0.043	$^{+0.011}_{-0.009}$	0.040	$^{+0.008}_{-0.007}$
-1.005	0.042	$^{+0.008}_{-0.007}$	0.026	$^{+0.006}_{-0.006}$	0.039	$^{+0.010}_{-0.009}$	0.029	$^{+0.011}_{-0.004}$
-0.754	0.066	$^{+0.011}_{-0.010}$	0.043	$^{+0.007}_{-0.007}$	0.069	$^{+0.012}_{-0.011}$	0.072	$^{+0.009}_{-0.011}$
-0.503	0.124	$^{+0.016}_{-0.014}$	0.089	$^{+0.019}_{-0.012}$	0.130	$^{+0.024}_{-0.025}$	0.118	$^{+0.013}_{-0.018}$
-0.251	0.341	$^{+0.030}_{-0.052}$	0.325	$^{+0.030}_{-0.040}$	0.270	$^{+0.037}_{-0.027}$	0.276	$^{+0.034}_{-0.024}$
0.000	0.661	$^{+0.060}_{-0.050}$	0.819	$^{+0.046}_{-0.050}$	0.512	$^{+0.046}_{-0.046}$	0.641	$^{+0.032}_{-0.030}$
0.251	0.256	$^{+0.032}_{-0.025}$	0.303	$^{+0.048}_{-0.027}$	0.284	$^{+0.033}_{-0.047}$	0.333	$^{+0.024}_{-0.034}$
0.503	0.106	$^{+0.019}_{-0.014}$	0.103	$^{+0.016}_{-0.022}$	0.124	$^{+0.023}_{-0.024}$	0.121	$^{+0.012}_{-0.014}$
0.754	0.065	$^{+0.012}_{-0.012}$	0.041	$^{+0.008}_{-0.008}$	0.062	$^{+0.011}_{-0.011}$	0.045	$^{+0.009}_{-0.006}$
1.005	0.035	$^{+0.006}_{-0.008}$	0.021	$^{+0.006}_{-0.004}$	0.035	$^{+0.010}_{-0.006}$	0.026	$^{+0.008}_{-0.004}$
1.257	0.019	$^{+0.006}_{-0.006}$	0.025	$^{+0.006}_{-0.007}$	0.023	$^{+0.005}_{-0.006}$	0.036	$^{+0.005}_{-0.007}$
1.508	0.022	$^{+0.005}_{-0.007}$	0.021	$^{+0.007}_{-0.004}$	0.029	$^{+0.007}_{-0.006}$	0.027	$^{+0.007}_{-0.004}$
1.759	0.024	$^{+0.007}_{-0.005}$	0.037	$^{+0.006}_{-0.007}$	0.066	$^{+0.016}_{-0.018}$	0.042	$^{+0.008}_{-0.006}$
2.011	0.039	$^{+0.011}_{-0.007}$	0.046	$^{+0.010}_{-0.012}$	0.233	$^{+0.034}_{-0.055}$	0.095	$^{+0.009}_{-0.015}$
2.262	0.080	$^{+0.013}_{-0.013}$	0.106	$^{+0.012}_{-0.026}$	0.425	$^{+0.076}_{-0.049}$	0.195	$^{+0.016}_{-0.026}$
2.513	0.352	$^{+0.031}_{-0.048}$	0.258	$^{+0.028}_{-0.035}$	0.363	$^{+0.064}_{-0.039}$	0.440	$^{+0.042}_{-0.027}$
2.765	0.675	$^{+0.046}_{-0.041}$	0.439	$^{+0.058}_{-0.026}$	0.144	$^{+0.020}_{-0.020}$	0.335	$^{+0.021}_{-0.033}$
3.016	0.249	$^{+0.027}_{-0.027}$	0.248	$^{+0.022}_{-0.029}$	0.051	$^{+0.010}_{-0.012}$	0.117	$^{+0.017}_{-0.010}$

Table 4: Energy-flow distribution in the three-jet plane, normalised to the total invariant mass, as a function of the azimuthal angle, ϕ^*, in the different regions of the (ξ, x_1) plane.

$\frac{d\sigma}{d\eta^*_{\rm jet}}$ (pb)			
$d\eta^*_{\rm jet}$	$\frac{d\sigma}{d\eta^*_{\rm jet}}$ (pb)	(stat.) (pb)	(stat. $\bigoplus$ syst.) (pb)
[-3.6,-3.0]	0.650	$\pm$0.121	$^{+0.250}_{-0.185}$
[-3.0,-2.4]	2.167	$\pm$0.228	$^{+0.335}_{-0.352}$
[-2.4,-1.8]	4.279	$\pm$0.333	$^{+0.972}_{-0.557}$
[-1.8,-1.2]	8.193	$\pm$0.465	$^{+1.493}_{-1.034}$
[-1.2,-0.6]	10.322	$\pm$0.526	$^{+1.162}_{-0.841}$
[-0.6,0.0]	9.384	$\pm$0.506	$^{+0.940}_{-0.958}$
[0.0,0.6]	7.132	$\pm$0.429	$^{+0.704}_{-0.856}$
[0.6,1.2]	8.359	$\pm$0.445	$^{+1.295}_{-0.837}$
[1.2,1.8]	9.417	$\pm$0.471	$^{+1.171}_{-0.857}$
[1.8,2.4]	9.543	$\pm$0.605	$^{+1.241}_{-1.338}$
[2.4,3.0]	1.039	$\pm$0.145	$^{+0.381}_{-0.203}$

Table 5: Differential cross section for three-jet production as a function of the jet pseudorapidity, $d\sigma/d\eta^*_{\rm jet}$, of the three jets.

$\frac{d\sigma}{dP^*_{\rm T,jet}}$ (pb/GeV)			
$dP^*_{\rm T,jet}$ (GeV)	$\frac{d\sigma}{dP^*_{\rm T,jet}}$ (pb/GeV)	(stat.) (pb/GeV)	(stat. $\bigoplus$ syst.) (pb/GeV)
[1.0,3.0]	3.970	$\pm$0.182	$^{+0.521}_{-0.333}$
[3.0,5.0]	2.291	$\pm$0.136	$^{+0.378}_{-0.244}$
[5.0,7.0]	0.818	$\pm$0.090	$^{+0.143}_{-0.175}$
[7.0,9.0]	0.172	$\pm$0.039	$^{+0.058}_{-0.070}$

Table 6: Differential cross section for three-jet production as a function of the jet transverse momentum, $P^*_{\rm T,jet}$, of the most-forward jet.

$\rho(\varphi)$						
	$\rho(\varphi)$ (most-forward jet)			$\rho(\varphi)$ (most-backward jet)		
$d\varphi$ (radians)	$\rho(\varphi)$	(stat.)	(stat. $\bigoplus$ syst.)	$\rho(\varphi)$	(stat.)	(stat. $\bigoplus$ syst.)
[0.0,0.2]	1.524	$\pm$0.057	$^{+0.086}_{-0.083}$	2.188	$\pm$0.063	$^{+0.084}_{-0.119}$
[0.2,0.4]	1.500	$\pm$0.042	$^{+0.057}_{-0.061}$	1.273	$\pm$0.038	$^{+0.127}_{-0.054}$
[0.4,0.6]	0.877	$\pm$0.029	$^{+0.043}_{-0.053}$	0.721	$\pm$0.030	$^{+0.044}_{-0.063}$
[0.6,0.8]	0.473	$\pm$0.020	$^{+0.053}_{-0.026}$	0.350	$\pm$0.017	$^{+0.024}_{-0.034}$
[0.8,1.0]	0.300	$\pm$0.015	$^{+0.022}_{-0.019}$	0.219	$\pm$0.013	$^{+0.019}_{-0.023}$
[1.0,1.2]	0.165	$\pm$0.010	$^{+0.018}_{-0.013}$	0.125	$\pm$0.009	$^{+0.015}_{-0.011}$
[1.2,1.4]	0.103	$\pm$0.008	$^{+0.010}_{-0.015}$	0.069	$\pm$0.006	$^{+0.010}_{-0.007}$
[1.4,1.6]	0.047	$\pm$0.005	$^{+0.007}_{-0.008}$	0.025	$\pm$0.003	$^{+0.008}_{-0.005}$

Table 7: The differential jet shape, $\rho(\varphi)$, for the most-forward and most-backward jets with $E^*_{\rm jet} > 9$ GeV in three-jet events, where the Pomeron defines the forward direction.